What Maintains the SST Front North of the Eastern Pacific Equatorial Cold Tongue?*

SIMON P. DE SZOEKE AND SHANG-PING XIE

International Pacific Research Center, University of Hawaii at Manoa, Honolulu, Hawaii

TORU MIYAMA

Frontier Research Center for Global Change, Japan Agency for Marine-Earth Science and Technology, Yokohama, Japan

KELVIN J. RICHARDS AND R. JUSTIN O. SMALL

International Pacific Research Center, University of Hawaii at Manoa, Honolulu, Hawaii

(Manuscript received 19 April 2006, in final form 6 September 2006)

ABSTRACT

A coupled ocean–atmosphere regional model suggests a mechanism for formation of a sharp sea surface temperature (SST) front north of the equator in the eastern Pacific Ocean in boreal summer and fall. Meridional convergence of Ekman transport at 5°N is forced by eastward turning of the southeasterly cross-equatorial wind, but the SST front forms considerably south of the maximum Ekman convergence. Geostrophic equatorward flow at 3°N in the lower half of the isothermally mixed layer enhances mixed layer convergence.

Cold water is upwelled on or south of the equator and is advected poleward by mean mixed layer flow and by eddies. The mixed layer current convergence in the north confines the cold advection, so the SST front stays close to the equator. Warm advection from the north and cold advection from the south strengthen the front. In the Southern Hemisphere, a continuous southwestward current advects cold water far from the upwelling core.

The cold tongue is warmed by the net surface flux, which is dominated by solar radiation. Evaporation and net surface cooling are at a maximum just north of the SST front where relatively cool dry air is advected northward over warm SST. The surface heat flux is decomposed into a response to SST alone, and an atmospheric feedback. The atmospheric feedback enhances cooling on the north side of the front by 178 W m^{-2}, about half of which is due to enhanced evaporation from cold dry advection, while the other half is due to cloud radiative forcing.

1. Introduction

The Hadley circulation is the first-order circulation of the Tropics. The southeasterly and northeasterly trade winds in the planetary boundary layer (PBL) converge onto the low pressure region over the warmest sea surface temperature (SST) (Gill 1980; Lindzen and Nigam 1987; Neelin 1989), forming a zonal band of atmospheric convergence and rain known as the intertropical convergence zone (ITCZ). The warmest SST in the eastern Pacific Ocean is found during September in a zonal band around 10°–15°N (Fig. 1a). In September the seasonal solar heating reinforces the background meridional temperature gradient, with warmer temperatures in the Northern Hemisphere. This meridional asymmetry is maintained through most of the year by air–sea feedbacks. [See Xie (2004) for a comprehensive review of the these air–sea interaction mechanisms.] The SST asymmetry drives the southeasterly trade winds across the equator into the Northern Hemisphere. These strong winds cool the tropical South Pacific by enhancing surface evaporation. In the ITCZ winds are much weaker, allowing the SST to stay warm. The southeasterly trades blow nearly parallel to the

* International Pacific Research Center Contribution Number 436 and School of Ocean Engineering Science and Technology Contribution Number 7056.

Corresponding author address: S. P. de Szoeke, NOAA/ESRL/PSD3, 325 Broadway, Boulder, CO 80304.
E-mail: Simon.deSzoeke@noaa.gov

DOI: 10.1175/JCLI4173.1

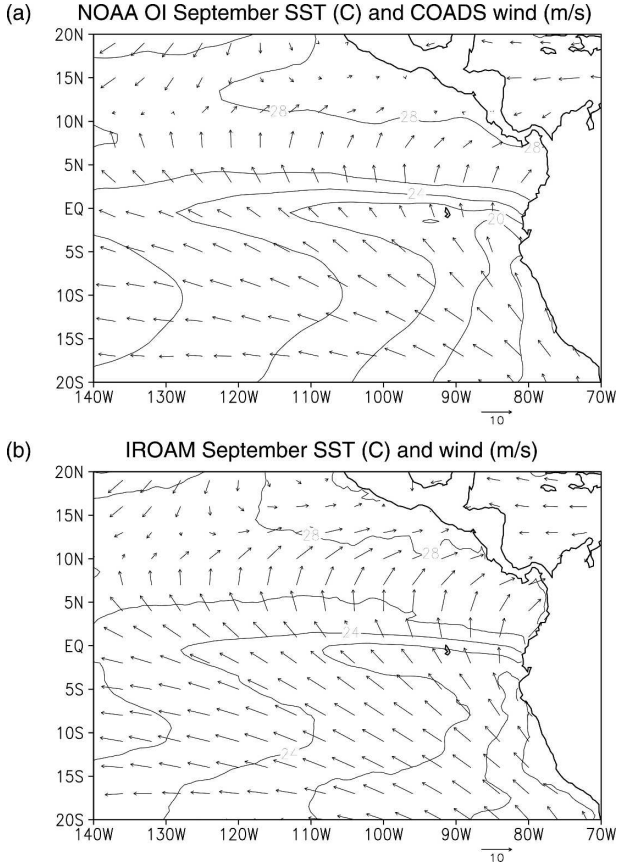

FIG. 1. (a) NOAA optimally interpolated SST (°C) for September averaged over 1998–2003. Vectors show the September COADS surface wind climatology. (b) IROAM 1998–2003 September averaged SST (°C) and surface wind. The length of the arrow at the lower right is for a 10 m s^{-1} wind.

coast of Peru, driving coastal upwelling. Extensive low clouds reduce the SST in the tropical South Pacific by reducing solar radiation at the surface.

During September, the equatorial cold tongue of SST is well developed with a sharp front to its north separating it from the eastern Pacific warm pool. By contrast, the gradient on the southern flank of the cold tongue is much weaker. This study explores the reasons for the relative strength of the meridional SST gradient on either side of the cold tongue.

In pioneering research, Cromwell (1953) documented meridional–vertical sections of tracers observed in the upper equatorial Pacific Ocean and inferred upwelling of dense water at the equator and downwelling at a surface front north of the equator. The front separated dense phosphate-rich equatorial water from light oxygen-rich water to the north. Cromwell proposed that wind-driven surface currents could generate a front near the equator. Lacking a reliable wind climatology, he noted that uniform southerly winds would drive convergent currents north of the equator between the (nonrotating) northward frictional current at the equator and the eastward Ekman current in the north.[1] Easterly trade winds on the equator are responsible for equatorial divergence and upwelling.

Philander and Pacanowski (1981) modeled the effect of the cross-equatorial winds on the ocean. The northward wind drags the northward current across the equator, contributing to surface current divergence and upwelling slightly south of the equator and current convergence and downwelling to the north. The linear equatorial ocean response to southerly wind contributes equatorial upwelling in addition to the upwelling driven by the zonal trade winds (McCreary 1985).

Kessler et al. (1998) modeled the seasonal evolution of the eastern Pacific equatorial cold tongue with an ocean general circulation model, and Wang and McPhaden (1999) diagnosed the seasonal cycle of the equatorial heat budget from Tropical Atmosphere Ocean (TAO) Array mooring observations. These works show that cooling in April–August is due to strong upwelling and zonal advection and warming in boreal winter is due to weak upwelling and meridional advection. The present study is limited to September, when the SST is a minimum on the equator. The temperature tendency is small, so ocean circulation must maintain the SST gradient against damping by the surface flux.

Our knowledge of eastern Pacific winds has improved substantially since the Cromwell (1953) study. In late boreal summer, southeasterlies prevail in the Southern Hemisphere and cross the equator (Fig. 1a). North of the equator, the wind turns eastward and converges on the ITCZ north of 10°N. On the eastern equator, the wind is directed northward parallel to the Ecuadorian shore. Figure 2 is a schematic illustration of currents generated by these winds. Veering wind generates convergent Ekman current in the Northern Hemisphere. South of the equator, divergence of the current results in upwelling of cold water, indicated in Fig. 2 by the arrow out of the page. The wind drives cold water across the equator as far as 6°N where the wind is northward and Ekman transport is eastward. The SST front in Fig. 1b is considerably south of the wind-driven transport centered at 5°N. Hence the line of convergence of the wind-driven current does not explain the location of the SST front. This paper presents

[1] The term "Ekman current" refers to a solution of the frictional Ekman model without pressure adjustment. "Wind-driven current" is the generalized frictional current in the upper ocean. For finite Coriolis parameter f off the equator, the wind-driven current approaches the Ekman current.

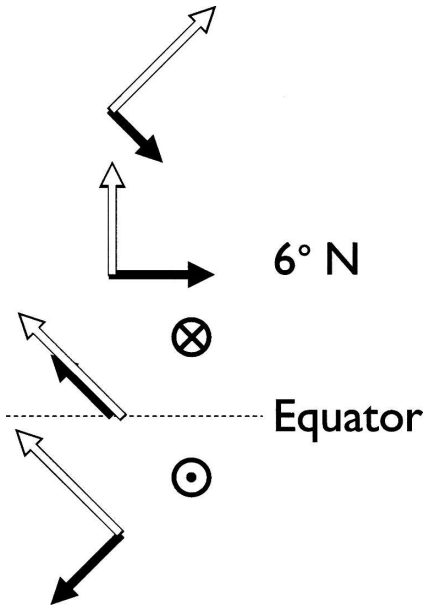

FIG. 2. Schematic of wind-driven current convergence resulting from the observed wind stress (white arrows) in late boreal summer. Wind-driven ocean transports are indicated by the black arrows.

a comprehensive examination of processes in the ocean and atmosphere that maintain and destroy the large-scale SST gradient north of the cold tongue.

The SST front creates a number of important features in the atmosphere, including increased wind speed and a low cloud band just north of the front (Wallace et al. 1989; Deser et al. 1993; Chelton et al. 2001; de Szoeke and Bretherton 2004; Small et al. 2005). The decreased solar radiation and increased turbulent heat flux cool the ocean north of the SST front, while relatively clear skies and low winds warm the cold tongue. The SST front exists between the equator and 2°N, despite the nearly 200 W m^{-2} difference in net surface flux that warms the cold tongue and cools the warm water to the north (de Szoeke et al. 2005). The surface fluxes damp the SST front, so the mechanism for frontogenesis must lie in the ocean. As discussed above, the details of the mechanism remain unclear.

The present study investigates the oceanic frontogenesis and associated atmospheric feedback using a newly developed coupled ocean–atmosphere model of the eastern Pacific. The model realistically represents the surface wind and SST climatology (Fig. 1b) and it is free to develop coupled ocean–atmosphere feedbacks. We limit our attention to September, when the equatorial SST is at a climatological minimum. We show that upwelling at the equator is a source of cold water, which is transported poleward by the mixed layer current. A SST front forms in the north where the northward advection of cold water stops. South of the cold tongue, the SST gradient is weak because the mixed layer current continues to carry cold water southward.

Previous studies have focused on tropical instability waves (TIWs) that propagate westward along the SST front (Legeckis 1977). Hansen and Paul (1984), using satellite-tracked buoys, and Bryden and Brady (1989), using moored current measurements, estimated that TIW heat transport onto the equator is on the order of the heat transport by Ekman divergence. Other studies (e.g., Cox 1980; Kessler et al. 1998; Jochum et al. 2005; Menkes et al. 2006) have modeled TIWs and shown their heating contribution at the equator. The role of TIWs in creating or destroying the SST gradient is more ambiguous. The waves displace the front and blur the Eulerian mean gradient, but the instantaneous gradient is still strong. Jochum and Murtugudde (2006) argue from model results that in proximity to the line source of equatorial upwelling, sinuous advection of SST by TIWs can sharpen the SST gradient on length scales shorter than the TIWs.

Recently other mechanisms for small-scale ocean frontogenesis have been proposed. Wijesekera and Paulson (2006, manuscript submitted to *J. Mar. Res.*) suggest that the curvature of the zonal current drives convergence in the nonlinear Sverdrup transport at the equatorial front. Thomas and Lee (2005) propose a frontogenesis mechanism by which Ekman transport from wind blowing along an SST front induces buoyancy-driven ageostrophic circulations that converge on the front, amplify the frontal jet, and are unstable through nonlinear Ekman feedback with the atmosphere. Frontogenesis by this mechanism seems to occur on scales shorter than 10 km, while the resolution of our ocean model is 50 km. These mechanisms could be taking place in the ocean below the scale of the TIWs but, since the front is remarkable even after averaging over the eddies, we turn our attention to the mean conditions that contribute to the large-scale front.

Section 2 introduces the coupled ocean–atmosphere model. Section 3 presents the upper-ocean circulation in the coupled model and proposes mechanisms for the maintenance of the cold tongue front in the eastern Pacific. Section 4 presents a heat budget averaged over the depth of the ocean mixed layer. The mixed layer heat budget shows the importance of upwelling and advection of cold water away from the cold tongue. Section 5 presents the surface heat fluxes on the ocean, whose sum tends to warm the cold tongue and cool the warm SST in the Northern Hemisphere. The atmospheric temperature, humidity, wind, and cloud radiative forcing respond to SST and affect surface fluxes. In section 6, the surface fluxes are decomposed into a

component that depends solely on the SST and a component that is due to the atmospheric adjustment as it blows across the SST front. Section 7 summarizes our findings.

2. A coupled model of the eastern tropical Pacific region

The International Pacific Research Center (IPRC) Regional Ocean Atmosphere Model (IROAM: Xie et al. 2007) simulates coupled ocean–atmosphere processes in the eastern Pacific Ocean. The IROAM consists of the Geophysical Fluid Dynamics Laboratory Modular Ocean Model version 2 (MOM2: Pacanowski 1995), for the Pacific basin from 35°S to 35°N, coupled to the IPRC Regional Atmospheric Model (RAM: Wang et al. 2003) from 150° to 30°W between 35°S and 35°N. Surface winds, humidity, temperature, and radiative fluxes over the western part of the Pacific Ocean are prescribed by the daily National Centers for Environmental Prediction–National Center for Atmospheric Research (NCEP–NCAR) reanalysis (Kistler et al. 2001), and turbulent fluxes are computed from a bulk formula (Fairall et al. 2003). The lateral boundaries of the RAM are nudged toward four-times daily NCEP–NCAR reanalysis. The influence of the land surface of the Americas is modeled by the Biosphere–Atmosphere Transfer Scheme (BATS: Dickinson et al. 1993), and the SST of the Atlantic Ocean is prescribed to the RAM from the weekly Reynolds et al. (2002) optimally interpolated SST. The ocean and the atmosphere models have horizontal resolution of $0.5° \times 0.5°$. The MOM2 has 30 z-coordinate levels, 15 between the surface and 200 m. MOM2 uses a constant lateral diffusivity of heat and momentum of 200 $m^2\,s^{-1}$. Vertical mixing is computed with the Pacanowski and Philander (1981) parameterization, with a minimum vertical diffusivity of 10^{-6} $m^2\,s^{-1}$. Overturning of unstable water columns is achieved by the Cox (1984) explicit convection scheme.

The MOM2 is initialized with Levitus (1982) climatology in January 1991, spun up for five years with NCEP boundary conditions, and then coupled to the RAM in January 1996. Fluxes of heat and momentum are computed every time step by the RAM using the Coupled Ocean–Atmosphere Response Experiment (COARE: Fairall et al. 2003) bulk flux algorithm. Heat and momentum fluxes are averaged daily and updated daily to the MOM2, and the SST is updated daily to the RAM.

We allow the coupled IROAM to spin up for two years before analyzing the output. IROAM "climatology" is averaged for each calendar month for the six years 1998–2003. This period excludes the strong El Niño of 1997. The results are changed little by extending the average over 1997.

Figure 1b shows the IROAM September climatology of SST and wind vectors in the eastern Pacific. The SST pattern is quite similar to the NOAA optimally interpolated SST (Fig. 1a). The strength and westward extent of the cold tongue and the temperature of the cold upwelled water off the South American coast are realistic. The SST front is stronger to the east in both the observations and the model. The 26°C isotherm shifts northward unrealistically at 100°W in the model, west of which the cold tongue front is more diffuse than observed.

The IROAM wind is similar to observations. The modeled wind speed has a minimum over the cold tongue, but is too strong by 1–2 $m\,s^{-1}$ compared to observations. The modeled winds are stronger in the Northern Hemisphere and more westerly in the ITCZ than observed. These wind errors could be related to an overestimate of ITCZ precipitation (Xie et al. 2007), especially along the southwest coast of Central America.

3. Coupled simulation of the equatorial cold tongue with IROAM

Figure 3a shows the currents in the top grid layer of the ocean model (0–10 m). South of 3°N the westward South Equatorial Current (SEC) is evident. The eastward North Equatorial Countercurrent (NECC) is north of 5°N. In IROAM, west of 110°W, northward currents exceeding 60 $cm\,s^{-1}$ feed the southern flank of the NECC. Observations of surface currents (Johnson et al. 2001) show that the maximum meridional current averaged between 170° and 95°W is only 13 $cm\,s^{-1}$ at 4°N. [The central Pacific average, appearing in Johnson et al., has nearly easterly wind stress and more symmetric overturning about the equator than the eastern Pacific. The observation closest to the surface is at 20-m depth; the surface current is extrapolated from the current observations at 20–30-m depth, so may not accurately represent the surface current.]

Such strong northward surface currents are not generated when the MOM2 is forced by the NCEP surface wind (not shown). The NCEP cross-equatorial wind is known to be weaker than observed, especially in September (Wu and Xie 2003). Nevertheless, the IROAM wind speed is about 1–2 $m\,s^{-1}$ too strong. The strong northward current in the coupled IROAM is the Ekman response to the stronger-than-observed wind stress. West of 100°W the northward current in IROAM displaces the 26°C isotherm 1°–2° north relative to observations.

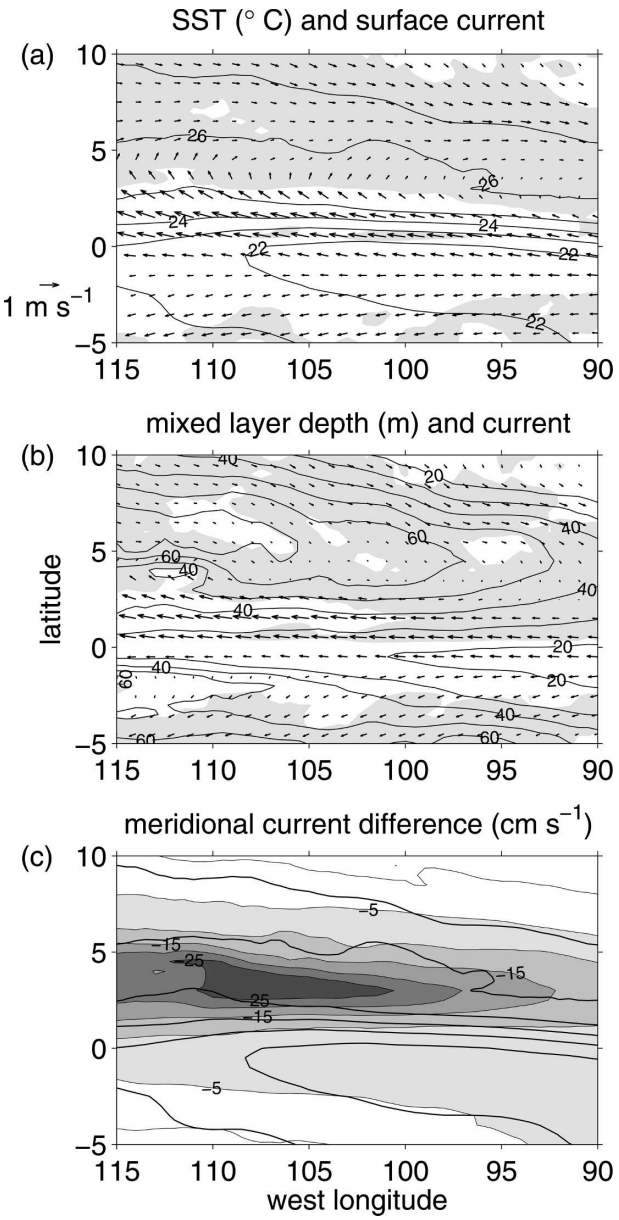

FIG. 3. (a) IROAM SST (contours: °C) and surface current $\mathbf{u}_0$ vectors. The meridional convergence is shaded above 5×10^{-6} s^{-1}. (b) Mixed layer depth h (contour interval: 10 m) and mixed layer averaged velocity $\langle \mathbf{u} \rangle$. (c) Mixed layer–surface current differences (cm s^{-1}, shaded).

The classical Ekman and geostrophic solutions are not valid on the equator. Therefore, we analyze numerical solutions of the primitive equations from IROAM. Without theoretical rigor, we describe the qualitative likeness of the numerical solutions to Ekman and geostrophic idealizations.

Fronts will develop in the presence of meridional gradients and meridional current convergence. The eastward turning of the wind between the equator and the ITCZ drives convergent Ekman transport. The turning of the surface current results in a band of meridional convergence at 3°–6°N, shown by the shaded contours in Fig. 3a. The convergence at 3°–6°N in Fig. 3a is north of the strongest SST gradient. The SST gradient is relatively weak at 5°N and strongest between the equator and 2°N, where the surface current is weakly divergent.

A deeper look reveals that the surface current is not representative of current throughout the surface mixed layer. Rather, there is considerable shear in an isothermal layer. Hereafter we refer to this isothermally mixed layer simply as the "mixed layer" even though momentum is not mixed in the layer. A meridional–vertical cross section of the temperature and meridional current for the upper 100 m of the IROAM ocean along 95°W is shown in Fig. 4. There are 10 model layers between the surface and 100 m. Gray shading shows temperature, with cold water upwelling to the surface at the equator. The surface mixed layer is evident where temperature contours are nearly vertical. The meridional gradient of SST is confined near the equator.

The meridional currents in Fig. 4 show a northward lens at the surface centered at 2°N. This is consistent with Ekman drift to the right of the westward wind stress in the Northern Hemisphere. At the equator, in the absence of rotation, the wind-driven drift is in the direction of the northward wind stress. Below the surface, currents are strongly southward in the mixed layer. In the Northern Hemisphere the southward flow is in geostrophic balance with the pressure gradient from the westward increase in the sea surface height (Johnson et al. 2001; Niiler et al. 2003; Maximenko and Niiler 2005). Geostrophic and wind-driven flow combine near the surface. North of 6°N the Ekman transport is southward. The southward currents affect the surface temperature distribution by temperature advection in the mixed layer.

Since vertical mixing occurs rapidly compared to horizontal temperature advection in the mixed layer, we assume that temperature in the mixed layer is always effectively mixed, and the vertical average of velocity in the mixed layer advects the mixed layer average temperature $\langle T \rangle$, where angle brackets represent a vertical average from the surface to the depth of the mixed layer. The mixed layer depth h is defined as the depth at which the ocean temperature is 0.5°C cooler than the surface temperature. The advection of cold equatorial water by the northward surface current above warm water from the southward current (Fig. 4) causes unstable stratification and vertical overturning where the water masses meet at 1°–3°N. An internal tally of the heat source in the top 50 m of the model shows that convective overturning is responsible for in-

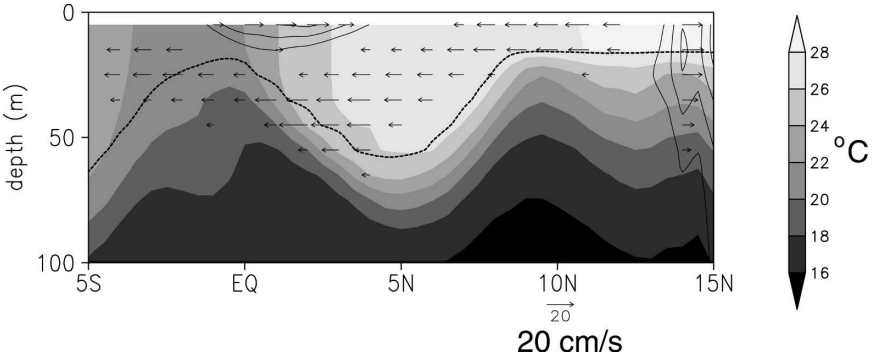

FIG. 4. IROAM meridional–depth section of temperature (°C: shaded) and meridional current (arrows) along 95°W for September 1998–2003. The reference arrow indicates a meridional current of 20 cm s^{-1}; currents less than 5 cm s^{-1} are not shown. Northward currents are contoured at 5, 10, and 15 cm s^{-1}. The base of the mixed layer is indicated by the dotted line.

termittent warming between the equator and 5°N. The mixed layer depth is indicated by the dotted line in Fig. 4. It roughly follows the depth of the thermocline along 95°W, shoaling at the equator and deepening at 5°N.

The mixed layer current $\langle \mathbf{u} \rangle$ is shown for the region 5°S–10°N, 115°–90°W in Fig. 3b. The mixed layer current tends to parallel mixed layer depth contours, which approximately scale as the thermocline depth, emphasizing its geostrophic nature. Because the Coriolis force disappears on the equator, identification of Ekman transport or geostrophic current can only be qualitative. We note that the surface current is dominated by the wind stress, while the mixed layer current reflects the wind stress and the pressure gradient.

Advection by the mixed layer current generates a SST front more than would advection by the surface current. We analyze means of sharpening the SST gradient, exploiting the zonal uniformity of the SST and the flow. If surface fluxes relax the ocean toward an equilibrium surface temperature T_E, at which evaporation balances radiative absorption, then the balance between advection and surface flux can be idealized,

$$vT_y = -\alpha(T - T_E). \tag{1}$$

A corollary for the temperature gradient can be found differentiating meridionally,

$$vT_{yy} = -(v_y + \alpha)T_y, \tag{2}$$

in which atmospheric damping of the gradient is offset by current convergence ($v_y < 0$).

The front is initially generated at the equator y_0, where water upwells and is initially far from equilibrium with the atmosphere. If the velocity v is constant, (1) implies that T exponentially approaches T_E with latitude. The meridional profile of SST, meridional surface current v_0, and mixed layer current $\langle v \rangle$ along 95°W are shown in Fig. 5. The mixed layer velocity is 5 cm s^{-1} at the equator and zero at 2°N. If we assume that the velocity v is converging between the equator and a latitude of equilibrium y_E, then the surface temperature T linearly approaches T_E. The Newtonian damping coefficient α estimated from the width of the front (~2°) and the velocity at the equator $v(y_0)$ is $\alpha = 2.3 \times 10^{-7}\ s^{-1} \approx (51\ \text{day})^{-1}$. For a mixed layer depth of 30 m and $T(y_0) = T_E - 4$°C, this damping coefficient implies a flux of 114 W m^{-2} at the equator, in line with the observed flux.

The mixed layer current generates an SST gradient because it is smaller and more convergent than the surface current. The reduction of the meridional velocity of the mixed layer relative to the surface is shown in Fig. 3c. Smaller advection reduces the length scale of

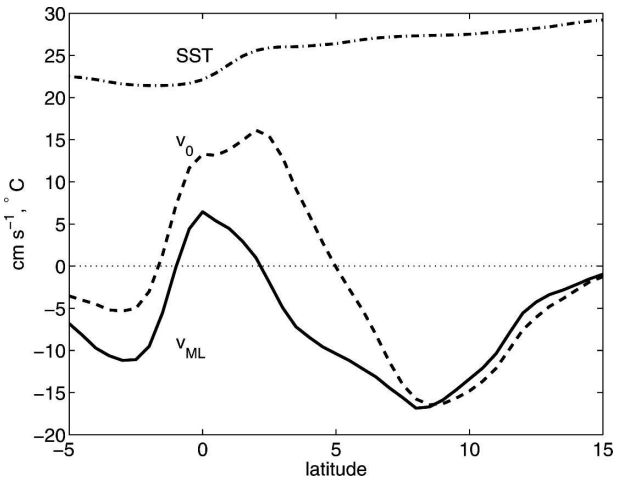

FIG. 5. IROAM SST (dot–dashed), surface current v_0, and mixed layer average meridional velocity $\langle v \rangle$ (solid) along 95°W.

adjustment in (1) and (2). Meridional mixed layer convergence in the front increases by $\sim 5 \times 10^{-7}$ s^{-1} relative to the surface, changing the sign of the convergence (shaded in Figs. 3a,b) in the eastern part of the front. The convergence difference causes the mixed layer current to sharpen the SST gradient by 0.08°C (° latitude)$^{-1}$ day^{-1} more than the surface current at 100°W.

Ekman transport from the clockwise-turning wind stress drives convergence at 4°–6°N. Absent equatorial upwelling, water from both sides of the convergence is warm and does not form a front. Once TIWs grow to significant amplitude in the west, their cold cusps reach 4°–6°N and curl around clockwise. South of the cusps the SST gradient reverses, with cold water to the north. Warm water converges meridionally from the sides and the cold water descends. Our analysis cannot distinguish whether the TIWs are causing convergence or responding to the wind-driven convergence here.

The minimum SST south of the equator clearly corresponds to divergence in the surface and mixed layer velocity. The SST front is located between the equator and 2°N. While meridional surface velocity v_0 diverges, mixed layer velocity $\langle v \rangle$ converges between the equator and 2°N. The difference between the surface and the mixed layer current between the equator and 5°N shows the importance of southward geostrophic flow in the mixed layer. At 2°–3°N the northward mixed layer velocity stops and is met by southward velocity from the north.

4. A mixed layer heat budget

The SST front is located in a region of weak northward meridional current (Fig. 3b). In this section we compute the mixed layer heat budget for September, which demonstrates the relative roles of horizontal advection, upwelling, and surface turbulent and radiative flux in maintaining the SST front. To first order upwelling in the cold tongue is balanced by solar heating. Horizontal advection enhances the front by warming its north side.

The temperature tendency equation used by the ocean model is

$$\frac{\partial T}{\partial t} = -\mathbf{u} \cdot \boldsymbol{\nabla} T + \boldsymbol{\nabla} \cdot (\kappa \boldsymbol{\nabla} T) + (\rho C_P)^{-1} \frac{\partial R}{\partial z} - Q_E - Q_H. \tag{3}$$

The first term on the right-hand side is three-dimensional advection, the second is diffusion, and the third is convergence of the net radiative heat flux. The ocean model has penetrative solar radiation and assumes that surface longwave radiation is entirely absorbed and emitted at the top model layer. The evaporative and sensible heat fluxes also converge in the surface layer; Q_E is the temperature sink due to surface evaporation and Q_H is due to the sensible heat flux. The fluxes R, E, and H are all defined positive downward. The effect of the explicit convection scheme, which vertically redistributes heat to mix out buoyant instability, is applied separately from the temperature equation and is not considered here.

The terms in (3) are computed for each model grid cell from daily averaged temperature, velocity, diffusivity, and surface flux. To compute the heat budget for the ocean mixed layer, the terms in (3) are vertically averaged over the mixed layer depth h. The mixed layer depth h: $T(-h) = T(0) - 0.5$ is computed from the daily data and then averaged over a month. The average mixed layer depth $\overline{h}$ is taken to be a constant throughout each month. We expect the ignored explicit convection to have only a small effect on the vertically integrated budget. The September climatologies presented are the average of six Septembers from 1998 to 2003. We separate the advection

$$\overline{\mathbf{u} \cdot \boldsymbol{\nabla} T} = \overline{\mathbf{u}} \cdot \boldsymbol{\nabla} \overline{T} + \overline{\mathbf{u}' \cdot \boldsymbol{\nabla} T'}, \tag{4}$$

into advection by the monthly mean and by the eddies, respectively, where the overline represents the monthly mean.

Figure 6a shows zonal advection of the mixed layer mean temperature by the monthly mean zonal current. A zonal temperature gradient exists because the temperature front is zonally tilted (cf. Fig. 1) with warmer temperature to the east. The zonal tilt of the front is because the southerly component of the wind increases to the east. The southerly wind component shifts the center of upwelling south of the equator. In the west, where the winds are more zonal, the center of upwelling is nearer the equator. The strong westward South Equatorial Current (SEC) in the SST front region advects warm water from the east into the front region with warming of 1°–3°C month^{-1}. Zonal advection is strong enough to change the sign of the total horizontal advection to warming north of the equator (Fig. 6). South of the equator the gradient is reversed and zonal advection cools about half as strongly as meridional advection. The zonal advection and local SST gradient do not necessarily imply advection of parcels all the way from the South American coast. Traveling at the mean mixed layer current of -30 cm s^{-1}, it would take more than a month for water to traverse 10° of longitude in which time its temperature would likely be damped by surface fluxes.

The September mixed layer mean meridional velocity advects cold upwelled water from the equator into

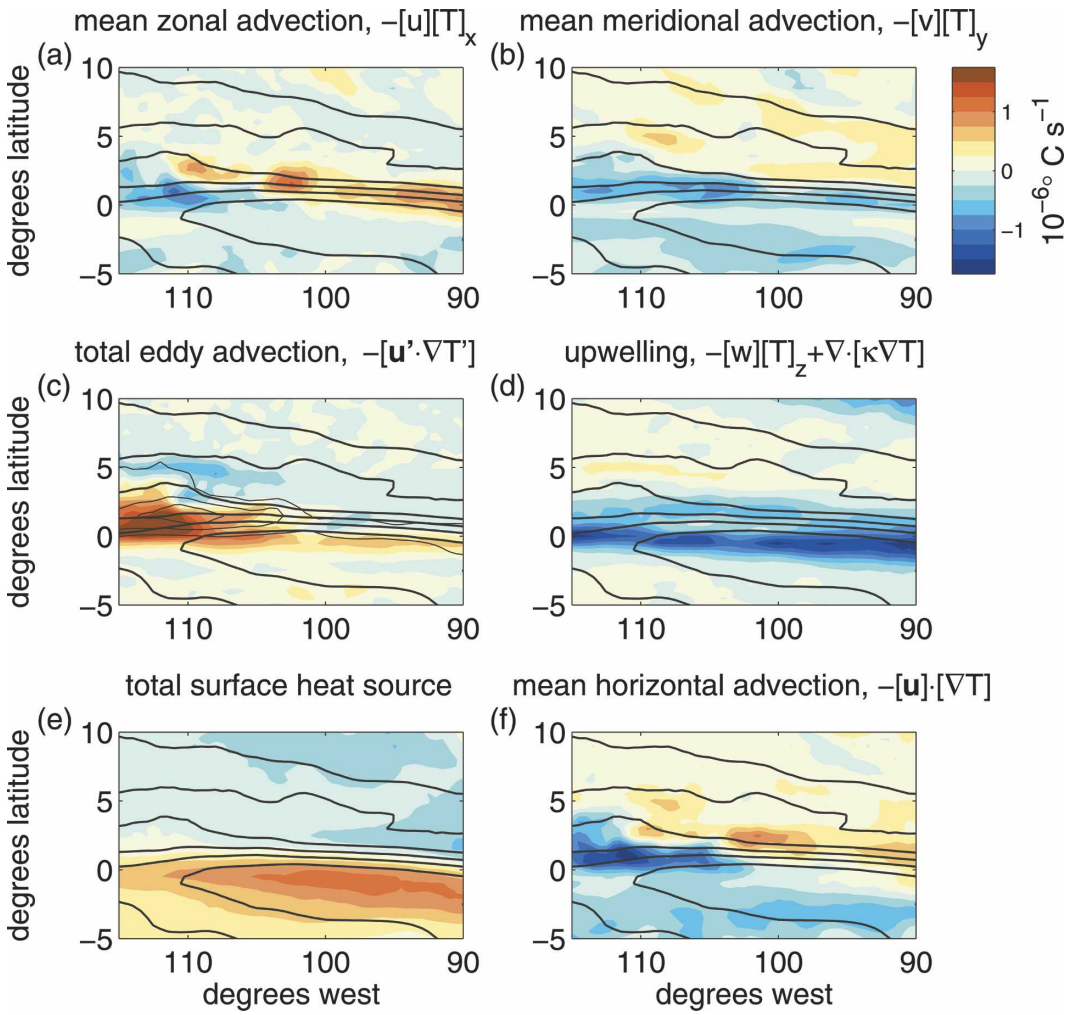

FIG. 6. IROAM sources to the mixed layer temperature budget in September: the (a) zonal and (b) meridional temperature advection in the mixed layer by the September mean current and temperature. (c) The total eddy advection. (d) The contribution of upwelling (the sum of diffusion and mean vertical advection) to the mixed layer temperature. (e) The total surface heat source from evaporation, sensible heat flux, and radiation. (f) The mean horizontal advection [sum of (a) and (b)]. For reference contours (interval 1°C) of mixed layer temperature $\langle T \rangle$ are overlaid. In (c) the thin contours are temperature variance [0.5(°C)^2].

the temperature front, cooling the front on its southern flank (Fig. 6b). The mean meridional current is relatively weak, but the temperature gradient is strong, resulting in a cooling comparable in magnitude to the zonal warming. Advection is strong because of the temperature gradient and acts to strengthen the gradient. North of the front there is weak warming from mean meridional advection because of southward advection by the mixed layer velocity. The zonal warming is shifted slightly to the north of the front, and the meridional cooling is shifted slightly to the south. Total mean horizontal advection (Fig. 6f) enhances the SST difference across the front by 1.5°C month^{-1}.

In the Southern Hemisphere, both zonal and meridional currents contribute to a broad region of cold advection, with its peak (−0.05°C day^{-1}) at 3°S. The continuity of the southward meridional mixed layer current into the Southern Hemisphere spreads cold water from the upwelling far to the south (Fig. 3b). In the Northern Hemisphere, meridional currents are weak and the cold water stays on the south side of the front.

Westward propagating tropical instability waves form along the temperature front between the equator and 5°N, 90°–115°W. Currents from these eddies meander north- and southward, advecting the SST front as they go. One or two TIWs propagate past a given point each month. In daily realizations, TIWs start to meridionally displace the 25°C isotherm between 100° and

105°W. TIWs grow as they propagate westward from 100°W, as indicated by the variance of the temperature (thin black contours, Fig. 6c). Though the instantaneous SST gradient is just as strong in the west, the meandering displacement of the SST front weakens the Eulerian monthly mean SST gradient.

The effect of TIWs on the mixed layer heat budget is captured by the eddy term, which is the sum of all horizontal and vertical temperature advection by the eddies. The eddies transport temperature across the frontal region and warm the core of the cold tongue. At 95°W there is a zonal band of warm advection along the equator and cold advection on the north side of the front. The dipole of temperature advection by the eddies grows and shifts northward as the TIWs grow west of 100°W (Fig. 6c). There is a large warming (>0.2°C day^{-1}) from the equator to 2°N and a small cooling at 5°N. Between the centers of warming and cooling, eddies weaken the mean SST gradient.

West of 100°W at 0°–2°N, mean meridional advection cooling doubles, and zonal advection cools because the temperature gradient reverses in the SEC north of the equator. The total mean horizontal advection (0.1°C day^{-1}, Fig. 6f) cancels half the eddy warming in the front. Mean horizontal advection warms around 5°N, partly compensating for the weakening of the front by eddies. Although TIWs weaken the front in the west, Fig. 6 does not suggest an entirely different mechanism for the front.

The contribution of upwelling to the mixed layer temperature is shown in Fig. 6d. The negative flux of temperature through the base of the mixed layer is achieved by a combination of vertical advection and diffusion. Vertical advection passes cold water through the thermocline to turbulent diffusion in the mixed layer. Small changes in the diagnosis of h will result in a compensation between vertical advection and diffusion with little effect on the net upwelling term. Upwelling generates a band of cooling north of the cold tongue core and south of the SST front. Here the SST, mixed layer depth, and thermocline depth are at a minimum. At 115°W, where winds are nearly easterly (Fig. 1), the maximum cooling is along the equator. To the east, the winds are more southerly, shifting the upwelling core slightly south of the equator. This southward shift of the upwelling is reflected in the southeastward tilt of the SST front. Despite the change in the wind direction, the SST front and upwelling are quite zonal and trapped on the equator. Upwelling cooling is balanced by warming from horizontal advection and surface fluxes (Fig. 7b). Around 5°N, there is warming from vertical advection, indicating that warm water is converging horizontally and displacing cold water through the base of the mixed layer.

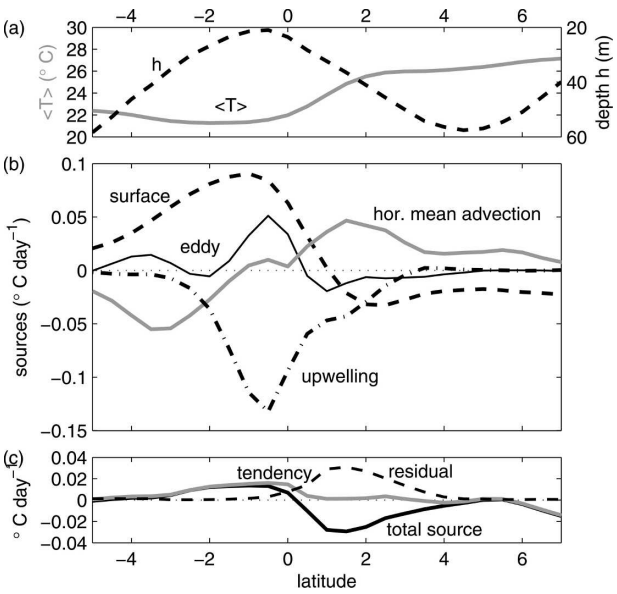

FIG. 7. The mixed layer heat budget averaged from 90° to 100°W. (a) The mixed layer temperature $\langle T \rangle$ (solid) and depth h (dashed). (b) The budget terms: surface flux divergence (including radiation; dashed), horizontal advection by the mean (solid gray), advection by eddies (thin black), and upwelling (the sum of diffusion and vertical advection; dot–dashed). (c) The sum of the sources (solid), the mixed layer temperature tendency (gray), and the residual (dashed).

The total convergence of the radiative, latent, and sensible heat flux from the surface of the mixed layer is shown in Fig. 6e. There is strong surface warming of the cold tongue. The cold SST reduces turbulent heat flux and relatively clear skies maximize the insolation of the ocean. Warming from surface flux divergence is enhanced by the shallow mixed layer along the equator. When surface flux is absorbed by a relatively shallow layer, the heating is greater. The change in sign of the total surface heat convergence coincides with the SST front. The change in surface heating across the front would tend to reduce the front by 3°C month^{-1}. North of the front, evaporation dominates insolation and the mixed layer loses heat to the atmosphere.

The patterns of diffusion, advection, and surface heating are all zonally oriented along the SST front and of comparable magnitude in the mixed layer heat budget. To synthesize the effect of all the terms in the heat budget, we have averaged surface heating (radiation and turbulent flux divergence), advection by the mean, advection by eddies, and diffusion between 90° and 100°W. The meridional profile of the mixed layer average temperature budget is presented in Fig. 7b. The upwelling term (dot–dashed) is the sum of diffusion

and mean vertical advection. Horizontal diffusion is two orders of magnitude smaller than vertical diffusion. On the equator surface heat flux (dashed) and advection by eddies (thin solid) are heating the mixed layer, while upwelling cools it. Meridional (zonal) advection cools (warms) the mixed layer along the temperature front (Figs. 6a,b). The net effect is that the mean horizontal advection (Figs. 6f and 7b) is small over the cold tongue and gradually increases from the equator to 0.05°C day^{-1} at 1.5°N. The mixed layer temperature sources at the equator in Fig. 7b are in agreement with those computed using TAO buoy observations on the equator at 110°W (Fig. 6 of Wang and McPhaden 1999).

The net surface flux follows the SST. Where SST is low, evaporation is small, and absorption of solar radiation causes a net warming. Where SST is high, evaporation increases and provides a net surface cooling to the ocean mixed layer. In this way surface flux restores the mixed layer temperature to an equilibrium at which evaporation balances solar absorption. Surface warming is very strong over the coldest water and decreases across the front as evaporative cooling increases over warmer SST beneath relatively cold and dry air.

The effect of eddies is to advect warm water into the cold tongue. Eddies warm the cold tongue by 0.05°C day^{-1}, consistent with the warming effect of TTWs as modeled by Kessler et al. (1998; 0.05°C day^{-1}), Jochum and Murtugudde (2006; 0.08°C day^{-1}), and Menkes et al. (2006; 0.07°C day^{-1}). The zonal average over 90°–100°W is in the region of TIW development. Where TIWs reach a larger amplitude farther west, they may play a larger role in the heat budget. The eddies also weakly cool the warm water north and south of the cold tongue, especially on the north side where the temperature front is sharper.

The eastern equatorial Pacific Ocean may be divided into three zonal regions based on the mixed layer temperature budget in Fig. 7b. In the cold tongue centered at 0.5°S, surface flux warming—dominated by radiative warming and to a lesser extent eddy warming—balance upwelling of cold water. South of 2°S, mean horizontal advection by the persistent southward current transports water from the cold tongue southward. Advection keeps this southern region cooler than its counterpart in the Northern Hemisphere. Moderate net surface flux balances cold advection in the south. In the Northern Hemisphere the poleward transport is weak and the advection of cold tongue water stops at the front. In the third region, north of 2°N, warm horizontal advection from the north and east balances net surface cooling. The front in the Northern Hemisphere marks the boundary at the northern limit of the transport of upwelled cold water.

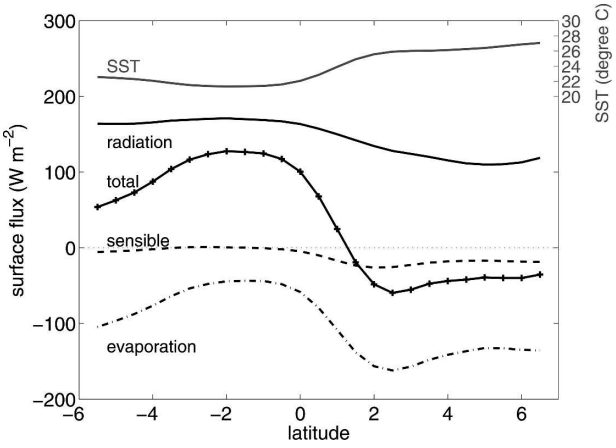

FIG. 8. Total surface heat flux into the ocean (W m^{-2}: marked with plus signs) along 90°–100°W and its constituents: radiative flux (solid), turbulent sensible heat flux (dashed), and turbulent evaporative heat flux (dot–dashed). Positive fluxes warm the ocean. The SST (gray solid) is included on a separate scale at the top of the figure for reference.

Figure 7a shows the mixed layer temperature $\langle T \rangle$ and depth h for reference. Figure 7c shows the sum of heat sources (black solid) in Fig. 7b and the tendency of the mixed layer temperature (gray solid). The residual (dashed) is the warming unexplained by the sum of the sources. The residual is small except in the vicinity of the SST front. At the front there is residual warming consistent with the effect of buoyant convective overturning from cold water overriding warm water and surface flux cooling at the SST front. Meridional currents become more equatorward with depth, as observed (Johnson et al. 2001), preventing cold water from sliding beneath warm water. In this unusual wind-driven circulation, the wind pushes dense water in the direction of light water, which acts to tilt density surfaces into the vertical. [This wind-driven buoyancy flux resembles the first step in the frontogenic instability of Thomas and Lee (2005), however the instability cannot exist in our model because the motion of the surface ocean current relative to the wind is not included in the wind stress.]

5. Surface heat fluxes: An atmospheric feedback

Sections 2–4 demonstrate how mixed layer velocity is important for the advection of heat in the mixed layer and how meridional convergence in the mixed layer creates conditions favorable for sharpening the SST gradient. This section investigates the atmospheric feedback of surface heat fluxes on SST.

The total surface heat flux and its components for the IROAM September (1998–2003) along 90°–100°W are shown in Fig. 8. Positive fluxes in Fig. 8 warm the

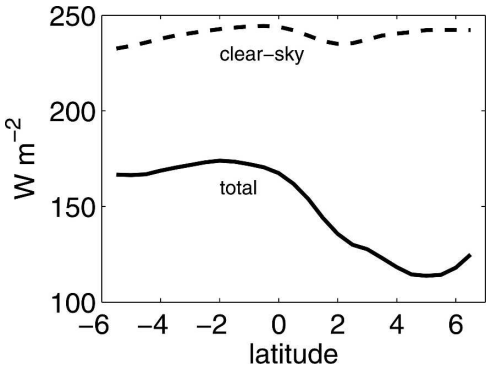

FIG. 9. Net September IROAM radiative heat flux into the ocean surface (solid) for 90°–100°W. The dashed line represents the radiative heat flux for clear-sky conditions; the difference between the total and the clear-sky flux is the cloud radiative forcing.

ocean. The total heat flux into the ocean is 120 W m^{-2} over the cold tongue, dropping sharply to zero just north of 1°N. Strongest surface cooling of the ocean occurs just to the warm side of the front at 2°–3°N and is a response to trade winds crossing the front. Evaporation, which varies with saturation specific humidity, relative humidity, and wind speed, is the main contributor cooling the ocean. The cold advection in the atmosphere enhances cooling downwind of the SST front.

The net radiative heat flux into the ocean for September is repeated in Fig. 9 (solid). The clear-sky radiative forcing is also shown. Under September equinoctial conditions, clear-sky radiative forcing is relatively constant, around 230 W m^{-2}. The clear-sky radiative forcing has a slight reduction north of the SST front where SST is warm and there is a thermal infrared "window" due to lack of water vapor in the atmosphere. The total radiative warming gradually shrinks north of the front as the cloud radiative forcing increases from −70 W m^{-2} over the cold tongue to −130 W m^{-2} at 5°N. Cloud radiative forcing in IROAM declines southward between the equator and 5°S. IROAM, like many coupled general circulation models, underestimates tropical southeastern Pacific stratus cloudiness. Satellite observations show that clouds increase south of 2°S.

Clouds increase with cold PBL air blowing over warm SST. The cold-advection PBL receives large moisture and buoyancy fluxes from the warm ocean surface. Immediately north of the SST front, stratiform clouds condense in the PBL (Deser et al. 1993). From the cold tongue to the ITCZ, stratiform clouds quickly give way to cumulus under stratocumulus and then to cumulus clouds (Norris 1998) as the boundary layer deepens over warming SST. This cloud transition was observed in the East Pacific Investigation of Climate 2001 experiment (EPIC: Raymond et al. 2004; Zeng et al. 2004; de Szoeke et al. 2005) and has previously been modeled with the IPRC Regional Atmospheric Model (Small et al. 2005) and with large eddy simulations (de Szoeke and Bretherton 2004).

From Fig. 8 the surface flux into the ocean is clearly larger over the cold tongue than over the warmer water to the north. The ocean surface temperature relaxes toward an equilibrium surface temperature T_E at which the evaporation balances the radiative absorption (Xie and Seki 1997). The upwelled water is cold, so the heat fluxes are out of equilibrium with a deficit of evaporation and a surplus of radiative warming heating the mixed layer. The water to the north is relatively well equilibrated. In fact, the flux north of the front cools the ocean slightly because of cold atmospheric advection from the south, warm oceanic advection from the north and the west, and negative cloud radiative forcing. The effect of adjustment of the PBL and clouds is examined in the next section.

6. A surface heat flux decomposition

In this section we introduce a decomposition of the surface turbulent heat flux. This decomposition divides the heat flux into a contribution from the ocean due to the change in SST and a contribution from the atmosphere as it advects and adjusts across the front. The ocean contribution to the flux is similar to the flux predicted by the Seager et al. (1988) model, which is often used as a thermodynamic boundary condition for ocean general circulation models.

The surface sensible heat flux H and evaporation E depend on the product of several quantities in the bulk formula,

$$H = \rho C_P C_H U(T - T_a) \tag{5}$$

$$E = \rho L C_E U[\gamma q^*(T) - \mathrm{RH} q^*(T_a)], \tag{6}$$

where ρ is the air density, C_H and C_E are bulk transfer coefficients for heat and moisture, C_P is the specific heat of air, L is the latent heat vaporization of water, U is the wind speed, T is the sea surface temperature, T_a is the surface air temperature, RH is the relative humidity of the surface air, and $q^*(T)$ is the Wexler function (or Clausius–Clapeyron relation) for the saturation specific humidity of water as a function of temperature. The factor $\gamma = 0.98$ parameterizes the reduction of saturation specific humidity over seawater relative to freshwater. Let

$$\Delta T = T_a - T \tag{7}$$

be the air–sea temperature difference, typically negative 1°–2°C in the Tropics. We decompose it into mean and perturbation quantities,

$$\Delta T = \overline{\Delta T} + \Delta T'. \tag{8}$$

The overbar mean represents a typical air–sea temperature difference, which for the following analysis is defined simply as the mean over 5°S to 6°N.

The relative humidity of the atmosphere RH is usually near 80%. In analogy to air–sea temperature difference, relative humidity and wind speed are decomposed $\mathrm{RH} = \overline{\mathrm{RH}} + \mathrm{RH}'$, and $U = \overline{U} + U'$. The saturation specific humidity of the air can be decomposed:

$$q^*(T_a) = q^*(T + \Delta T) = q^*(T + \overline{\Delta T}) + q^{*\prime} = \overline{q^*} + q^{*\prime}. \tag{9}$$

Assuming constant air–sea temperature difference $\overline{\Delta T}$, saturation specific humidity over the ocean $\overline{q^*} = q^*(T + \overline{\Delta T})$ depends only on the sea surface temperature T and not on the air temperature T_a. The term $q^{*\prime}$ can be linearized about $T + \overline{\Delta T}$,

$$q^{*\prime} \cong \Delta T' \left(\frac{\partial q^*}{\partial T} \right)_{T+\overline{\Delta T}}. \tag{10}$$

Cool atmospheric temperature anomalies increase evaporation by decreasing $q^{*\prime}$. The linearization introduces an error in the evaporation of less than 2% near the equatorial SST front, even where RH' and $\Delta T'$ are far from equilibrium.

Having defined atmospheric mean and perturbation quantities, we decompose surface evaporation E (6) into three terms:

$$E = \rho L C_E \overline{U}[\gamma q^*(T) - \overline{\mathrm{RH} q^*}] \tag{i}$$

$$+ \rho L C_E U'[\gamma q^*(T) - \overline{\mathrm{RH} q^*}] \tag{ii}$$

$$+ \rho L C_E U[-\overline{\mathrm{RH}} q^{*\prime} - \mathrm{RH}' q^*(T_a)], \tag{iii}$$

represented by the separate equation lines (i)–(iii). Line (i) depends only on the ocean and the difference from the ocean of mean atmospheric quantities. Even for constant air–sea temperature difference ΔT and relative humidity RH, variations in the ocean temperature affect the evaporation because the saturation specific humidity $q^*(T)$ is an exponential function of temperature. Lines (ii) and (iii) are forced by variations in the atmosphere. Line (ii) depends only on wind speed perturbations U' and the ocean temperature T. The thermodynamic atmospheric forcing (iii) depends on the full wind speed U, the perturbation air–sea temperature difference $\Delta T'$, and the perturbation relative humidity RH'.

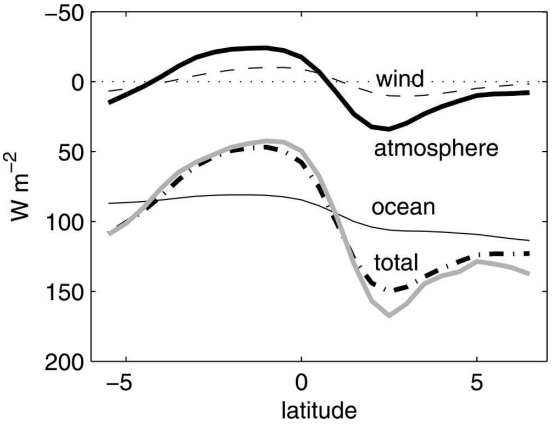

FIG. 10. Terms composing the surface evaporation E. The ocean term [(i): thin solid], the wind speed term [(ii): dashed], and atmospheric forcing term [(iii): thick solid] at 90°–100°W. The total evaporation [(i)–(iii)] is black dot–dashed and the evaporation computed by the IROAM is gray. Note: the ordinate is reversed so that positive evaporation (cooling the ocean) is plotted downward.

This decomposition of the evaporation is general. Here we choose specifically to apply it to the equatorial front north of the cold tongue where the sharp SST front and the sharp response of the atmosphere affect the heat fluxes. Figure 10 shows the three terms (i)–(iii) for 90°–100°W for the IROAM September climatology. Since the means of T_a, RH, and U are taken over latitude, the meridional mean of terms (ii) (dashed) and (iii) (thick solid) are zero—except for a small nonlinear contribution to the last term (iii). The ocean term (ii) (thin solid) increases only 27 W m^{-2} across the front, reflecting the increase in saturated specific humidity with increasing ocean surface temperature. The wind speed term increases 20 W m^{-2} across the front. The thermodynamic atmospheric forcing (iii) is 59 W m^{-2} larger on the north side of the front, reflecting the smaller relative humidity ($\mathrm{RH}' < 0$) and larger air–sea temperature difference ($\Delta T' < 0$, $q^{*\prime} < 0$) north of the front due to northward advection of cold and dry air from the equatorial cold tongue. Figure 10 also shows the sum of the three terms (i)–(iii) (black dot–dashed) and IROAM evaporation diagnosed each time step by the COARE (Fairall et al. 2003) bulk flux algorithm (gray). The monthly averages used for the offline flux decomposition are smooth compared to the instantaneous meridional sections of velocity, temperature, and humidity. The smoothing of the gradient results in weaker atmospheric advection on the north side of the front and underprediction of the peak flux north of the front.

The decomposition of the air–sea temperature difference can likewise be applied to the sensible heat flux

TABLE 1. Components of the heat flux difference (W m^{-2}) from 1°S to 2.5°N: ocean forcing of the evaporation E_{ocean}, total atmospheric forcing of the evaporation E_{atm}, sensible heat flux H_{atm}, and net downwelling radiation at the surface R.

Heat flux difference across 1°S–2.5°N				
E_{ocean}	E_{atm}	H_{atm}	R	Total
27	79	30	42	178

(not shown). The sensible heat flux depends linearly on the air–sea temperature difference ΔT, so the contribution from the mean is uniform over the region. The heat flux out of the ocean increases 28 W m^{-2} across the front due to the atmospheric adjustment $\Delta T'$ and increases 2 W m^{-2} due to the wind-driven component of the heat flux.

Table 1 shows the difference of the surface flux components between the cold tongue core and north of the front (1°S–2.5°N). The surface flux components are the ocean response to the change in the SST (E_{ocean}), the effect of the relative humidity, air temperature, and wind speed on the evaporation (E_{atm}), their effect on the sensible heat flux (H_{atm}), and the net radiative flux at the surface (R_0). All four terms in Table 1 contribute significantly to the surface flux difference across the front. The largest contributor is E_{atm}, the evaporation due to the cold, dry, and windy atmospheric anomaly north of the front.

7. Summary

Setting aside seasonal and interannual variability, we have described the conditions in the ocean mixed layer that maintain the sharp SST front north of the eastern Pacific cold tongue in September. We have diagnosed reasons for the strength and location of the SST front from IROAM, a coupled regional ocean–atmosphere model.

The relative roles of ocean dynamics, the response of the surface flux to SST, and the atmospheric feedback to the surface flux is summarized by Fig. 11. The ocean dynamics term (gray) is the sum of all advection and diffusion in the mixed layer—upwelling, horizontal advection, and eddy advection from Fig. 7. The ocean flux term (black dashed) includes the contribution of the SST to the evaporation through the saturation specific humidity, the mean sensible heat flux, and the net clear-sky radiative flux. The term from the atmosphere (black solid) includes the contribution to evaporation and sensible heat flux of departures in relative humidity, air–sea temperature difference, and wind speed from their typical values. The atmospheric forcing also

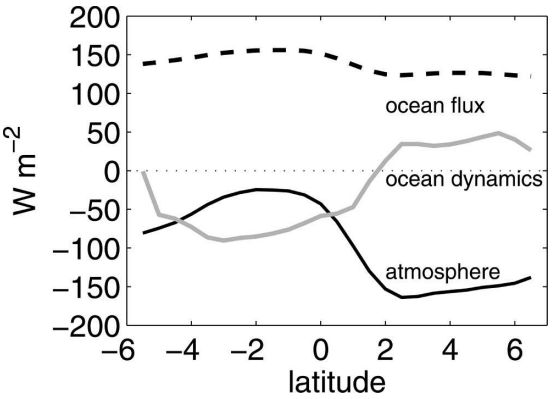

FIG. 11. A summary of important terms in the eastern tropical Pacific Ocean mixed layer heat budget. The ocean dynamical term (gray solid) is the sum of all advection and diffusion in the mixed layer. The ocean flux (dashed) contains the contribution to the heat flux that depends on SST and the clear-sky radiative warming. The atmosphere term (black solid) includes the contribution of departures from the mean air–sea temperature difference, relative humidity, and wind speed, and the cloud radiative forcing.

includes the cloud radiative forcing. The uniform offset of the ocean flux and the atmospheric flux terms is arbitrary and occurs because the radiative absorption is always positive, while the cloud radiative forcing is always negative.

Cold water wells up near the equator and advection and eddies distribute the cooling poleward. In the north, 40 W m^{-2} warm advection by the mean abuts the north edge of the SST front and cold water is held close to the equator. In the Southern Hemisphere currents transport cold water southward, resulting in cold advection of 50–90 W m^{-2}. The ocean flux changes 40 W m^{-2} in response to the SST change and clear-sky radiative forcing across the front. The dynamical ocean heat source is mostly compensated by atmospheric adjustment of the surface flux, which changes 150 W m^{-2} across the front. Cooling due to cloud radiative forcing, which gradually increases to the north, contributes almost half of the atmospheric cooling across the front in IROAM.

The SST front forms fundamentally as the boundary between cold, recently upwelled, water and warm water to the north, which has been in contact with strong tropical sunlight for a long time. The temperature at the surface reflects the temperature of a thermally mixed layer tens of meters deep. Within this mixed layer in the vicinity of the front there is mean vertical shear of the meridional current of 0.01 s^{-1}. The wind-driven surface flow is northward. Below the surface there is southward flow in response to the pressure gradients set up in the equatorial adjustment to the wind. This southward flow

contributes to the mean mixed layer velocity, moving the line of meridional convergence equatorward from 5° to 2°N and confining the meridional cold advection close to the equator. Owing to the orientation of the wind across the equator, the SST front is tilted northwest–southeast. The front is sharpened by zonal warm advection on its north side by the northern branch of the westward SEC.

In the Southern Hemisphere water from the cold tongue is advected southward by the meridional current. Meridional cold advection is reinforced by cold advection from the east by the SEC. Due to the continuous extension of cold advection, the SST gradient is weaker in the Southern Hemisphere.

Though the focus of this study has been on the mean conditions that maintain the SST front, the role of tropical instability waves is included in the eddy term of the mixed layer heat budget. The effect of eddies is to warm the cold tongue core and weakly to cool the front. A study of the heat budget of tropical instability waves by Jochum and Murtugudde (2006) shows that rather than mixing SST on diffusive scales, the waves spread cold water poleward by oscillatory advection, thereby allowing the surface flux to heat the ocean more efficiently. An IROAM simulation that damps eddies by increasing the lateral mixing (not shown) results in a broader and slightly colder cold tongue.

The surface sensible and evaporative heat flux has been decomposed into two terms: an oceanic term that responds identically to SST anywhere over the ocean and an atmospheric term that reflects departures of the atmospheric temperature, humidity, and wind speed from equilibrium with the ocean surface. The decomposition attributes the maximum ocean cooling seen on the north side of the front to strong advection of cold dry air across the SST front. This advection leads to strong evaporative and sensible cooling of the ocean. Positive wind speed anomalies further enhance evaporation and sensible heat flux north of the front. The decomposition of sensible heat flux and evaporation are general and can be performed on larger regions of the oceans of the globe. We expect the decomposition to yield similar results to the eastern Pacific equatorial front in regions of atmospheric cold advection, where strong heat fluxes cool the ocean.

Acknowledgments. We would like to acknowledge the insightful comments of Hyodae Seo, Billy Kessler, and two anonymous reviewers. This work has been funded by the Japanese Ministry of Education, Culture, Sports, Science and Technology (MEXT) as category 7 of the RR2002 Project. The numerical calculation was carried out at the Earth Simulator Center. The authors wish to acknowledge the support of the U.S. National Oceanic and Atmospheric Administration (NOAA) and the Japan Agency for Marine-Earth Science and Technology (JAMSTEC). We acknowledge Michael McPhaden for his useful comments, and Sharon DeCarlo, Yingshuo Shen, and Kazutoshi Horiuchi, who have diligently maintained our access to the IROAM data. COADS data can be downloaded from the ICOADS Web site (http://icoads.noaa.gov/) or the Asia Pacific Data Research Center Web site (http://apdrc.soest.hawaii.edu/).

REFERENCES

Bryden, H. L., and E. C. Brady, 1989: Eddy momentum and heat fluxes and their effect on the circulation of the equatorial Pacific Ocean. *J. Mar. Res.,* **47,** 55–79.

Chelton, D. B., and Coauthors, 2001: Observations of coupling between surface wind stress and sea surface temperature in the eastern tropical Pacific. *J. Climate,* **14,** 1479–1498.

Cox, M. D., 1980: Generation and propagation of 30-day waves in a numerical model of the Pacific. *J. Phys. Oceanogr.,* **10,** 1168–1186.

——, 1984: A primitive equation, 3-dimensional model of the ocean. GFDL Ocean Group Tech. Rep. 1, 143 pp.

Cromwell, T., 1953: Circulation in the meridional plane in the central equatorial Pacific. *J. Mar. Res.,* **12,** 196–213.

Deser, C., S. Wahl, and J. J. Bates, 1993: The influence of sea surface temperature gradients on stratiform cloudiness along the equatorial front in the Pacific Ocean. *J. Climate,* **6,** 1172–1180.

de Szoeke, S. P., and C. S. Bretherton, 2004: Quasi-Lagrangian large eddy simulations of cross-equatorial flow in the east Pacific atmospheric boundary layer. *J. Atmos. Sci.,* **61,** 1837–1858.

——, ——, N. A. Bond, M. F. Cronin, and B. M. Morley, 2005: EPIC 95°W observations of the eastern Pacific atmospheric boundary layer from the cold tongue to the ITCZ. *J. Atmos. Sci.,* **62,** 426–442.

Dickinson, R. E., A. Henderson-Sellers, and P. J. Kennedy, 1993: Biosphere-Atmosphere Transfer Scheme (BATS) version 1 as coupled to the NCAR Community Climate Model. NCAR Tech. Note TN-387+STR, 80 pp.

Fairall, C. W., E. F. Bradley, J. E. Hare, A. A. Grachev, and J. B. Edson, 2003: Bulk parameterization of air–sea fluxes: Updates and verification for the COARE algorithm. *J. Climate,* **16,** 571–591.

Gill, A. E., 1980: Some simple solutions for heat-induced tropical circulation. *Quart. J. Roy. Meteor. Soc.,* **106,** 447–462.

Hansen, D. V., and C. A. Paul, 1984: Genesis and effects of long waves in the equatorial Pacific. *J. Geophys. Res.,* **89,** 10 431–10 440.

Jochum, M., and R. Murtugudde, 2006: Temperature advection by tropical instability waves. *J. Phys. Oceanogr.,* **36,** 592–605.

——, ——, R. Ferrari, and P. Malanotte-Rizzoli, 2005: The impact of horizontal resolution in the tropical heat budget in an Atlantic Ocean model. *J. Climate,* **18,** 841–851.

Johnson, G. C., M. J. McPhaden, and E. Firing, 2001: Equatorial Pacific Ocean horizontal velocity, divergence, and upwelling. *J. Phys. Oceanogr.,* **31,** 839–849.

Kessler, W. S., L. M. Rothstein, and D. Chen, 1998: The annual

cycle of SST in the eastern tropical Pacific, diagnosed in an ocean GCM. *J. Climate,* **11,** 777–799.

Kistler, R., and Coauthors, 2001: The NCEP–NCAR 50-Year Reanalysis: Monthly means CD-ROM and documentation. *Bull. Amer. Meteor. Soc.,* **82,** 247–267.

Legeckis, R., 1977: Long waves in the eastern equatorial Pacific Ocean: A view from a geostationary satellite. *Science,* **197,** 1179–1181.

Levitus, S. E., 1982: *Climatological Atlas of the World Ocean.* NOAA Prof. Paper 13, 173 pp. and 17 microfiche.

Lindzen, R. S., and S. Nigam, 1987: On the role of sea surface temperature gradients in forcing low-level winds and convergence in the tropics. *J. Atmos. Sci.,* **44,** 2418–2436.

Maximenko, N. A., and P. P. Niiler, 2005: Hybrid decade-mean global sea level with mesoscale resolution. *Recent Advances in Marine Science and Technology, 2004,* N. Saxena, Ed., PACON International, 55–59.

McCreary, J. P., 1985: Modeling equatorial ocean circulation. *Annu. Rev. Fluid Mech.,* **17,** 359–409.

Menkes, C. E. R., J. G. Vialard, S. C. Kennan, J.-P. Boulanger, and G. V. Madec, 2006: A modeling study of the impact of tropical instability waves on the heat budget of the eastern equatorial Pacific. *J. Phys. Oceanogr.,* **36,** 847–865.

Neelin, J. D., 1989: On the interpretation of the Gill model. *J. Atmos. Sci.,* **46,** 2466–2468.

Niiler, P. P., N. A. Maximenko, and J. C. McWilliams, 2003: Dynamically balanced absolute sea level of the global ocean derived from near surface velocity observations. *Geophys. Res. Lett.,* **30,** 2164, doi:10.1029/2003GL018628.

Norris, J. R., 1998: Low cloud type over the ocean from surface observations. Part II: Geographical and seasonal variations. *J. Climate,* **11,** 383–403.

Pacanowski, R. C., 1995: MOM 2 documentation: User's guide and reference manual. Version 1.0, 232 pp.

——, and S. G. H. Philander, 1981: Parameterization of vertical mixing in numerical models of tropical oceans. *J. Phys. Oceanogr.,* **11,** 1443–1451.

Philander, S. G. H., and R. C. Pacanowski, 1981: The oceanic response to cross-equatorial winds (with application to coastal upwelling in low latitudes). *Tellus,* **33,** 201–210.

Raymond, D. J., and Coauthors, 2004: EPIC2001 and the coupled ocean–atmosphere system of the tropical east Pacific. *Bull. Amer. Meteor. Soc.,* **85,** 1341–1354.

Reynolds, R. W., N. A. Rayner, T. M. Smith, D. C. Stokes, and W. Wang, 2002: An improved in situ and satellite SST analysis for climate. *J. Climate,* **15,** 1609–1625.

Seager, R., S. E. Zebiak, and M. A. Cane, 1988: A model of the tropical Pacific sea surface temperature climatology. *J. Geophys. Res.,* **93,** 1265–1280.

Small, R. J., S.-P. Xie, Y. Wang, S. K. Esbensen, and D. Vickers, 2005: Numerical simulation of boundary layer structure and cross-equatorial flow in the eastern Pacific. *J. Atmos. Sci.,* **62,** 1812–1830.

Thomas, L. N., and C. M. Lee, 2005: Intensification of ocean fronts by down-front winds. *J. Phys. Oceanogr.,* **35,** 1086–1102.

Wallace, J. M., T. P. Mitchell, and C. Deser, 1989: The influence of sea-surface temperature on surface wind in the eastern equatorial Pacific: Seasonal and interannual variability. *J. Climate,* **2,** 1492–1499.

Wang, W., and M. J. McPhaden, 1999: The surface-layer heat balance in the equatorial Pacific Ocean. Part I: Mean seasonal cycle. *J. Phys. Oceanogr.,* **29,** 1812–1831.

Wang, Y., O. L. Sen, and B. Wang, 2003: A highly resolved regional climate model (IPRC-RegCM) and its simulation of the 1998 severe precipitation event over China. Part I: Model description and verification of simulation. *J. Climate,* **16,** 1721–1738.

Wu, R., and S.-P. Xie, 2003: On the equatorial Pacific surface wind changes around 1977: NCEP–NCAR reanalysis versus COADS observations. *J. Climate,* **16,** 167–173.

Xie, S.-P., 2004: The shape of continents, air-sea interaction, and the rising branch of the Hadley circulation. *The Hadley Circulation: Present, Past and Future,* H. R Diaz and R. S. Bradley, Eds., Kluwer Academic, 121–152.

——, and M. Seki, 1997: Causes of the equatorial asymmetry in sea surface temperature over the eastern Pacific. *Geophys. Res. Lett.,* **24,** 2581–2584.

——, and Coauthors, 2007: A regional ocean–atmosphere model for eastern Pacific climate: Toward reducing tropical biases. *J. Climate,* **20,** 1504–1522.

Zeng, X., M. A. Brunke, M. Zhou, C. Fairall, N. A. Bond, and D. H. Lenschow, 2004: Marine atmospheric boundary layer height over the eastern Pacific: Data analysis and model evaluation. *J. Climate,* **17,** 4159–4170.